Validating Plate Boundary Observatory borehole strainmeter data with GNSS derived strain

Trever T. Hines and Eric A. Hetland

July 27, 2017

1   Introduction

The Plate Boundary Observatory (PBO) contains 82 borehole strain meters (BSMs), most of which are installed along the western United States. BSMs are able to detect geophysical processes such as coseismic and postseismic deformation (e.g., Langbein et al., 2006; Langbein, 2015), slow slip events (SSEs) (e.g., Dragert and Wang, 2011), and seismic wave propagation (Barbour and Crowell, 2017). BSMs are intended for measuring deformation over timescales of minutes to months. At longer timescales, BSM data is contaminated by factors such as borehole relaxation (Gladwin et al., 1987). SSEs and postseismic deformation occur on timescales that near the upper limit of what BSMs can be expected to resolve. Another complication with BSM data is that the strain measured at the borehole may deviate from the regional strain due to local topographic or geologic features (Berger and Beaumont, 1976). Due to these sources of noise, it can be difficult to use BSM data quantitatively in, for example, geophysical inverse problems. In this study, we assess the ability of BSMs to measure strain resulting from SSEs on the Cascadia subduction zone. This is done by comparing BSM data to strain derived from GNSS data.

2   BSM Data

The are about forty PBO BSMs in the Pacific Northwest, and only five of them, B003, B004, B005, B007, and B018, record noticeable deformation from SSEs. We limit our attention to these five station in this study. The remaining stations either contain too much noise on the timescale of SSEs or are too far away from the SSEs to observe any strain. Each of the PBO BSMs are Gladwin four-component tensor strainmeters, which are about 2 m long, 8.7 cm in diameter, and are installed at about 100 to 200 m depth. Each BSM contains four extensometers, or gauges. Only three gauges are necessary to completely determine the horizontal strain tensor, and the fourth gauge is included for redundancy. Gauges 1, 2, and 3 are oriented 60°, 120°, and 150° counterclockwise from gauge 0.

We use the level 2 gauge data provided by UNAVCO at www.unavco.org, which has undergone several post-processing steps. In the level 2 gauge data a borehole curing trend is estimated and removed by fitting two exponential terms and a linear trend to the data. The level 2 data is corrected for tidal strains by estimating and removing sinusoids with known tidal frequencies. There is also a correction for barometric pressure because the normal stress imposed on the surface by barometric pressure results in horizontal strains recorded by the BSM. The barometric pressure correction is the observed barometric pressure at each site multiplied by a best fitting scaling factor. Lastly, offsets have been removed in the level 2 data product.

We denote the extension measured at gauge i as e_i, and the horizontal strain tensor components as ε_{xx}, ε_{yy}, and ε_{xy}, where x and y indicate the east and north direction, respectively. The extensions measured at BSMs are traditionally converted to areal strain, $\varepsilon_a = \varepsilon_{xx} + \varepsilon_{yy}$, differential strain, $\varepsilon_d = \varepsilon_{xx} - \varepsilon_{yy}$, and engineering shear strain, $\varepsilon_s = 2\varepsilon_{xy}$. We follow this convention and use ε_a, ε_d, and ε_s for comparing BSM data to GNSS derived strains. Using θ_0 to denote the orientation of gauge 0, in degrees north of east, these strain components can be expressed in terms of the gauge measurements through the equation

$$\begin{bmatrix} \varepsilon_a \\ \varepsilon_d \\ \varepsilon_s \end{bmatrix} = 2\mathbf{K}^{-1} \begin{bmatrix} 1 & \cos(2\theta_0) & \sin(2\theta_0) \\ 1 & \cos(2(\theta_0 + 60)) & \sin(2(\theta_0 + 60)) \\ 1 & \cos(2(\theta_0 + 120)) & \sin(2(\theta_0 + 120)) \\ 1 & \cos(2(\theta_0 + 150)) & \sin(2(\theta_0 + 150)) \end{bmatrix}^+ \begin{bmatrix} e_0 \\ e_1 \\ e_2 \\ e_3 \end{bmatrix}, \tag{1}$$

where "+" indicates the Moore-Penrose pseudoinverse and $\mathbf{K}$ is a coupling matrix describing how the instrument strains relate to the crustal strains (Hart et al., 1996). The components ε_a, ε_d, and ε_s represent crustal strains,

and e_i are instrument strains. We assume that BSMs are installed in homogeneous, isotropic rock, allowing us to write the coupling matrix as

$$\mathbf{K} = \begin{bmatrix} c & 0 & 0 \\ 0 & d & 0 \\ 0 & 0 & d \end{bmatrix}, \tag{2}$$

where c, and d are response factors that depend on the elastic properties of the instrument, the grout, and surrounding rock (Gladwin and Hart, 1985). Based on the analysis of Gladwin and Hart (1985), we use $c = 1.5$ and $d = 3.0$. UNAVCO, the organization responsible for maintaining the PBO BSMs and disseminating their data, use these same response factors for their final data products.

Local topographic or geologic features can cause $\mathbf{K}$ to have non-zero off diagonal elements. If possible, the components of $\mathbf{K}$ should be determined in-situ by calibrating the BSM data with a well known strain source, such as diurnal and semi-diurnal tides (Hart et al., 1996; Roeloffs, 2010; Hodgkinson et al., 2013). Hart et al. (1996) calibrated a BSM at Pinyon Flat, using the tidal strains recorded at a collocated laser strain meter. This calibration method is, of course, not possible for most PBO BSMs. Roeloffs (2010) and Hodgkinson et al. (2013) calibrated PBO BSMs using theoretical predictions of tidal strains (e.g., Agnew, 1997). This approach is still not adequate for BSMs near large local bodies of water, which can make it difficult to form an accurate theoretical estimate of tidal strains. As determined by Roeloffs (2010), the five BSM stations considered in this paper are too close to the Straight of Juan de Fuca to be accurately calibrated with tidal strains. Since in-situ calibration is not possible, we note that our choice for $\mathbf{K}$ is likely to be a significant source of error in BSM data. Another potential source of error is the assumed orientation for θ_0. This orientation is determined by a compass on the instrument, and it is possible that magnetic minerals in the surrounding rock can give the compass an incorrect reading.

3 GNSS derived strain

We compare the BSM strain components to transient strains estimated from GNSS data. Here we consider transient strains to be any deviation from the secular strain rate. We use daily GNSS displacement solutions for 94 continuous GNSS stations in the Pacific Northwest (Figure 1). This data has also been made available through UNAVCO. We convert the GNSS data to transient strains using Gaussian process regression (GPR) as described in Hines and Hetland (2017). With GPR, we select a prior spatio-temporal covariance model for the geophysical signal that we want to recover. Following Hines and Hetland (2017), we assume that our prior for displacements is a Gaussian process with zero mean, and covariance function described by

$$C_u((t,x),(t',x')) = \phi^2 T(t,t') X(x,x'), \tag{3}$$

where T is the Wendland covariance function

$$T(t,t') = \left(1 - \frac{|t-t'|}{\tau}\right)_+^5 \left(\frac{8|t-t'|^2}{\tau^2} + \frac{5|t-t'|}{\tau} + 1\right), \tag{4}$$

and X is the squared exponential covariance function

$$X(\vec{x}, \vec{x}') = \exp\left(\frac{-||\vec{x} - \vec{x}'||_2^2}{2\ell^2}\right). \tag{5}$$

The hyperparameters ϕ, τ, and ℓ control the amplitude, characteristic time-scale, and characteristic length-scale of the prior, respectively. Hines and Hetland (2017) found that the optimal hyperparameters for describing displacements from SSEs are roughly $\phi = 0.5$ mm, $\tau = 0.1$ yr, and $\ell = 100$ km. These parameters were chosen objectively using maximum likelihood methods; however based on our experience, this prior may not be sufficiently flexible to described all the observed data. Consequently, we explore using lower values for τ and ℓ and a higher value for ϕ. For each tested set of hyperparameters, we condition the prior with the observed GNSS data and visually compare the posterior displacements to the observations. We settle on the values $\phi = 1.0$ mm, $\tau = 0.05$ yr, and $\ell = 80$ km. With this final set of hyperparameters, we condition the prior with the GNSS data and then spatially differentiate the posterior displacements to obtain transient strain.

4 Results

We compare the BSM data to GNSS derived strains for eight SSEs in the Puget Sound region. The earliest SSE considered occurred in spring 2009 and the latest SSE occurred in winter 2017. The two datasets are in best agreement for the summer 2010 SSE, which is shown in Figure 2. The data for the remaining SSEs are included at the end of this manuscript in Figures 7 through 13. We only show the differential and engineering shear
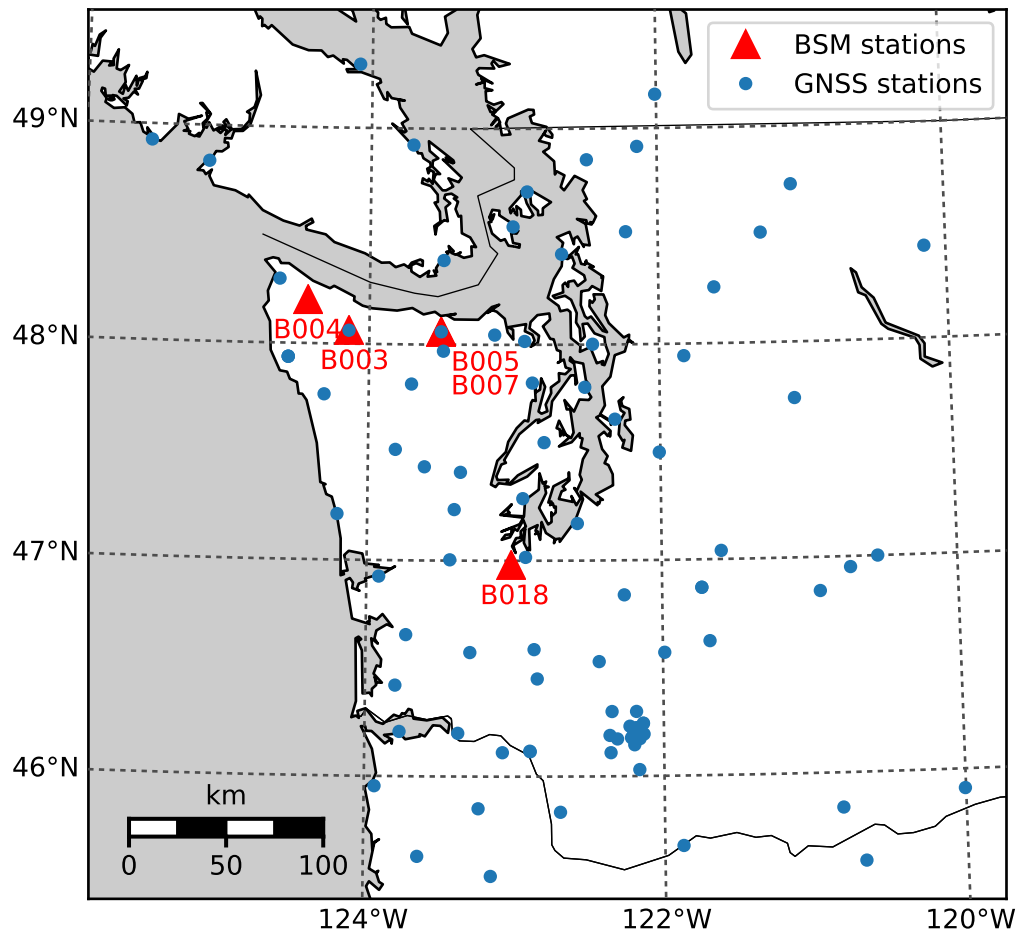
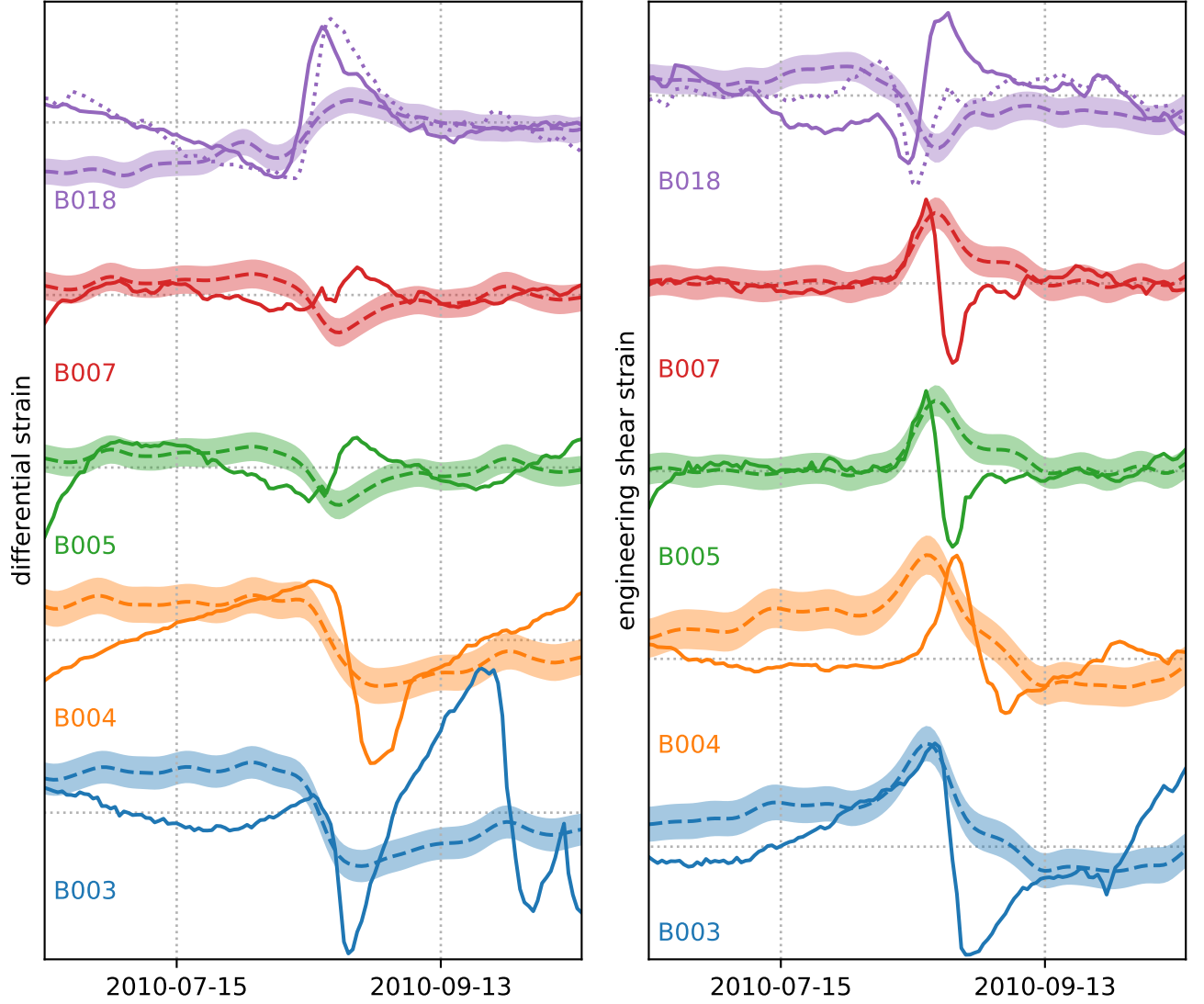Figure 1: Location of BSM and GNSS stations used in this study.

Figure 2: differential (left) and engineering shear (right) strains during the summer 2010 SSE observed at BSMs (solid) and derived from GNSS data (dashed). The horizontal dotted lines are spaced by 0.1 micro-strain. The shaded region around the GNSS derived strains show the one standard deviation confidence interval. The dotted line for station B018 shows the BSM data using the optimal instrument orientation. The shown BSM data has been detrended by estimating and removing a second-order polynomial from each timeseries.

strains because there is no clear signal in the areal strain for either the GNSS derived strains or the BSM data. Roeloffs (2010) also expressed doubt in the areal strains measured at stations B003, B004, B007, and B018 because the areal strains derived from different combinations of gauges at these stations are not self consistent. Roeloffs (2010) also noted an inconsistency in the differential strains at B003.

Station B004 records differential and engineering shear strains that are most consistent with the GNSS derived strains. However, the initiation of SSE strains recorded at B004 tend to lag several days behind the GNSS derived strains. The strain rates recorded at B004 also tend to be greater than the GNSS derived strains. One possible explanation for this discrepancy is that the GNSS station spacing is too wide to resolve a relatively sharp pulse of strain from the SSE as it traverses along the subduction zone.

The engineering shear strain, but not the differential strain, recorded at B003 contain a clear signal from each SSE that is consistent with the GNSS derived strains. Similar to B004, the recorded strain rates exceed those predicted by the GNSS data. There are many spurious features in the differential strains recorded at B003, which makes it difficult determine whether or not that component contains signal from SSEs.

Stations B005 and B007, which are located within a few hundred meters of each other, both show clear SSE signals in their engineering shear strains. However, the temporal pattern of strain recorded at these stations are not consistent with the GNSS derived strains. For the summer 2010 and summer 2011 SSEs, the GNSS derived strains predict a single positive pulse of engineering shear strain at these locations, but both B005 and
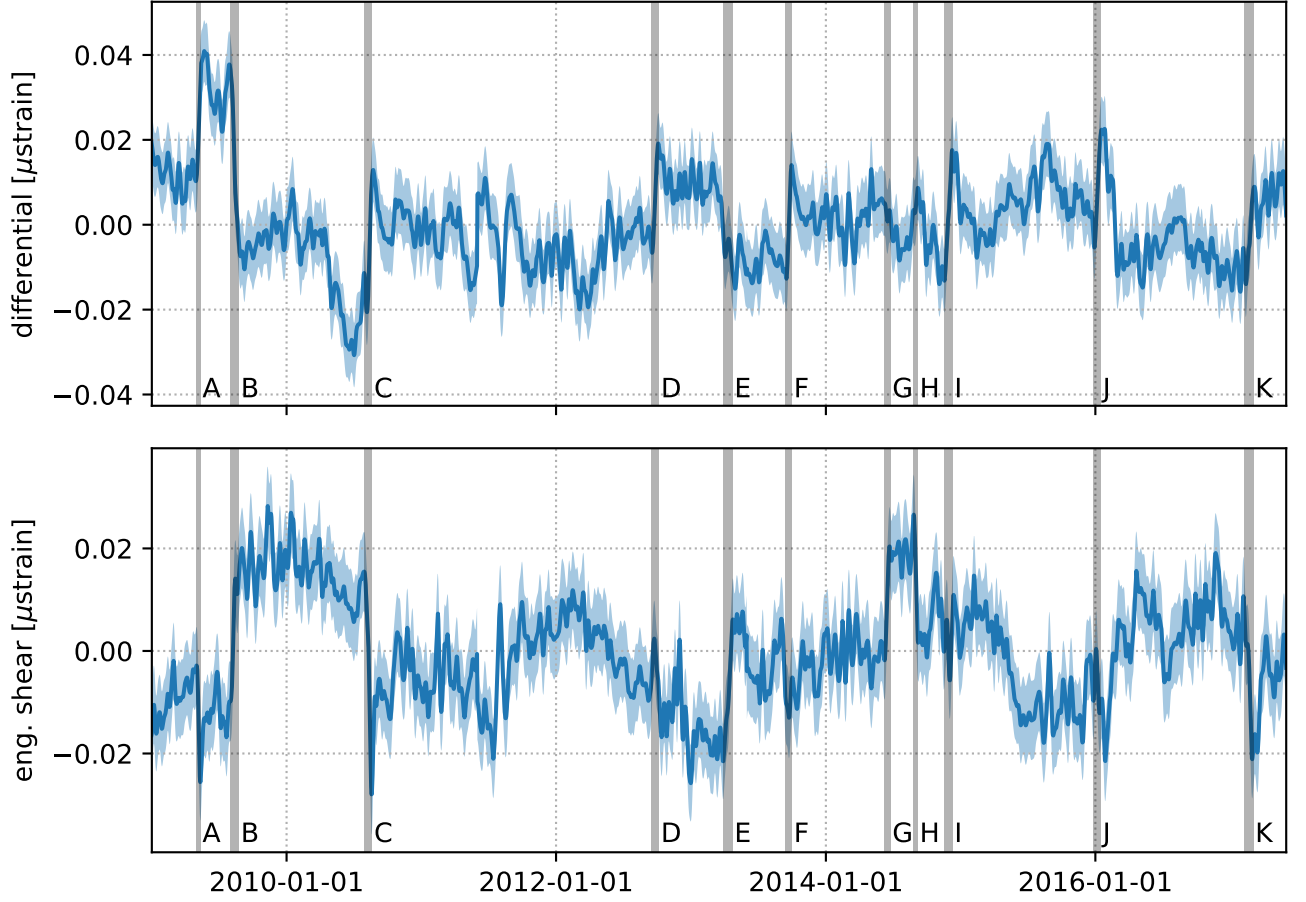
Figure 3: GNSS derived differential and engineering shear strains for station B018. The shaded blue regions indicate the one standard deviation confidence interval. The shaded gray regions indicate times of strain drops, which are the result of SSEs.

B007 record an initially positive pulse that then becomes negative. We cannot explain this discrepancy with mis-oriented instruments because both B005 and B007 would need to have nearly identical orientation errors. If the negative pulse of engineering shear strain were a regional ($\gtrsim$50 km scale) feature, then it would have been recognized in the GNSS data. We then suspect that the discrepancy can be explained with topographic of geologic features that may distort the local strain field. While, we are not saying that the engineering shear strains at B005 and B007 are erroneous, it is clear that they are inconsistent with the regional scale strains. The differential strains at station B005 and B007 do not show any clear SSE signal, even though a signal is observed in the GNSS derived strains. This too could be due to distortion of the strain field from local features.

The differential and engineering shear strains recorded at station B018 have notably less noise than most BSMs. Nonetheless, the engineering shear strains at B018 are not consistent with the GNSS derived strains. For example, BSM data shows a strain increase from the summer 2010 SSE, and the GNSS derived strains predict a strain decrease with about equal magnitude. We consider the possibility that this discrepancy is due to an error in the instrument orientation, and we identify a new, optimal orientation for station B018. We want to find the value for θ_0 that causes the strain drops (or increases) recorded at B018 to best match the strain drops derived from GNSS data. We identify 11 strain drops in the GNSS derived strains, which are due to SSEs in the Puget Sound region and in Oregon (Figure 3). We define strain drops as the total strain change over the hand-selected intervals shown in Figure 3. The strain drops for each event are shown in Figure 5. For each tested θ_0, we use eq. (1) to convert the strain drops recorded at each gauge (Figure 4) to the differential and engineering shear strain drops. We then use the L2 norm of the residuals, the difference between the BSM strain drops and the GNSS derived strain drops, as the misfit metric. We find an optimal value of θ_0 to be 293° east of north, which can be compared to the recorded value of 267° (Figure 6). With the new orientation, the engineering shear strain recorded at B018 decreases during the summer 2010 SSE, which is now consistent with the GNSS data (Figure 2). The differential strains at B018 are roughly consistent with the GNSS derived strains, regardless of whether the recorded θ_0 or optimal θ_0 is used.
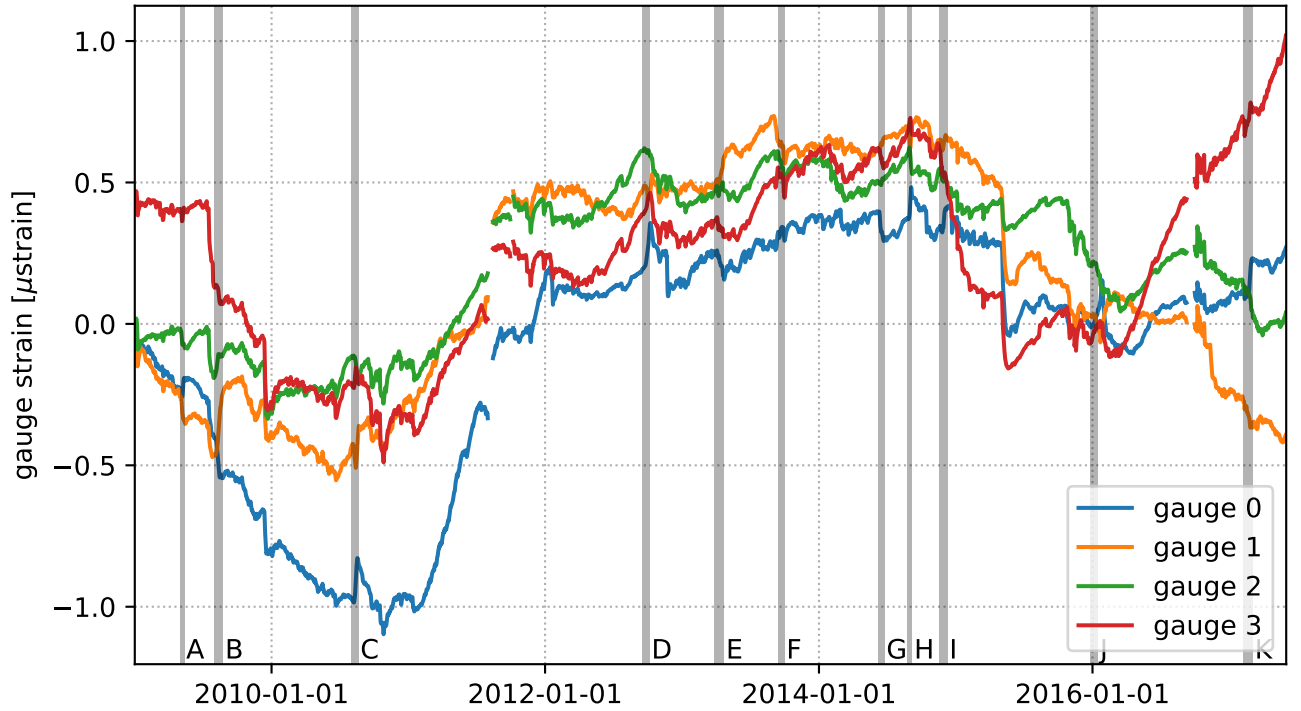
5

Figure 4: Gauge readings at station B018. The gray shaded regions indicate times of strain drops from Figure 3.

5   Conclusion

We have compared BSM data to GNSS derived strains for eight of the past SSEs in the Puget Sound region. The summer 2010 SSE produced the clearest signal in both the BSM data and GNSS derived strain, and yet it is still difficult to reconcile the two datasets. Of the five BSM stations that record strain from SSEs, only one of them, B004, records differential and engineering shear strains that are consistently in agreement with the GNSS derived strains. For station B003, only the engineering shear strains are consistent with the GNSS data. Both the differential and engineering shear strains recorded at B018 can be made to agree with the GNSS data when assuming a new instrument orientation. For station B005 and B007 it may be necessary to use a coupling matrix other than the isotropic one considered in this study. We are unaware of a reliable calibration method for these stations, since tidal calibration is not possible. In general, we urge caution when attempting to use BSM data to describe regional strains.

References

Agnew, D. C. (1997). NLOADF: A program for computing ocean-tide loading. *Journal of Geophysical Research*, 102:5109–5110.

Barbour, A. J. and Crowell, B. W. (2017). Dynamic Strains for Earthquake Source Characterization. *Seismological Research Letters*, 88(2A):354–370.

Berger, J. and Beaumont, C. (1976). An analysis of tidal strain observations from the United States of America II. The inhomogeneous tide. *Bulletin of the Seismological Society of America*, 66(6):1821–1846.

Dragert, H. and Wang, K. (2011). Temporal evolution of an episodic tremor and slip event along the northern Cascadia margin. *Journal of Geophysical Research: Solid Earth*, 116(12):1–12.

Gladwin, M. T., Gwyther, R. L., Hart, R., Francis, M., and Johnston, M. J. S. (1987). Borehole tensor strain measurements in California. *Journal of Geophysical Research: Solid Earth*, 92(B8):7981–7988.

Gladwin, M. T. and Hart, R. (1985). Design parameters for borehole strain instrumentation. *Pure and Applied Geophysics*, 123(1):59–80.
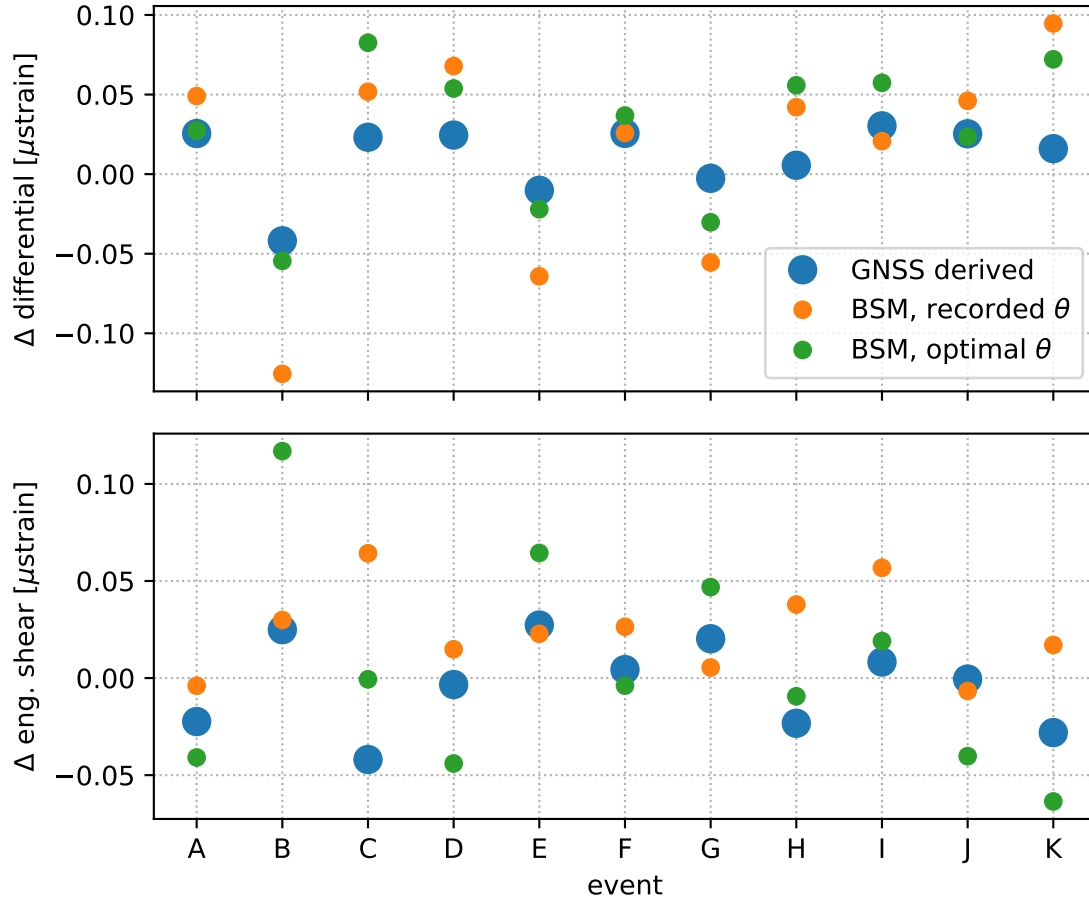
Figure 5: GNSS derived strain drops at station B018 during the 11 events identified in Figure 3 (blue dots), BSM strain drops using the recorded orientation for B018 (orange dots), and BSM strain drops using the optimal orientation for B018 (green dots).
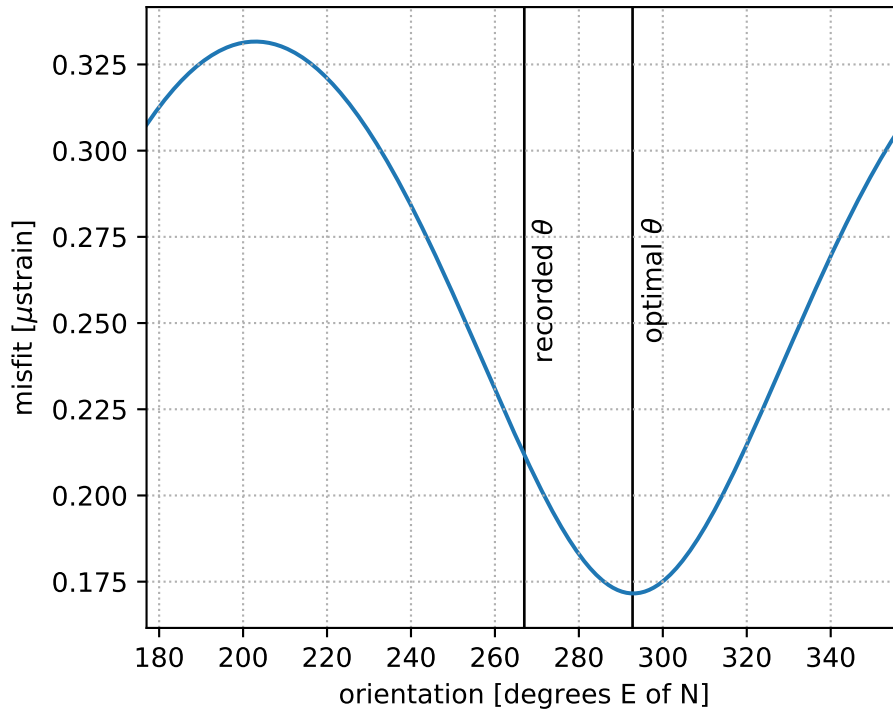

Figure 6: Misfit as a function of instrument orientation for station B018.
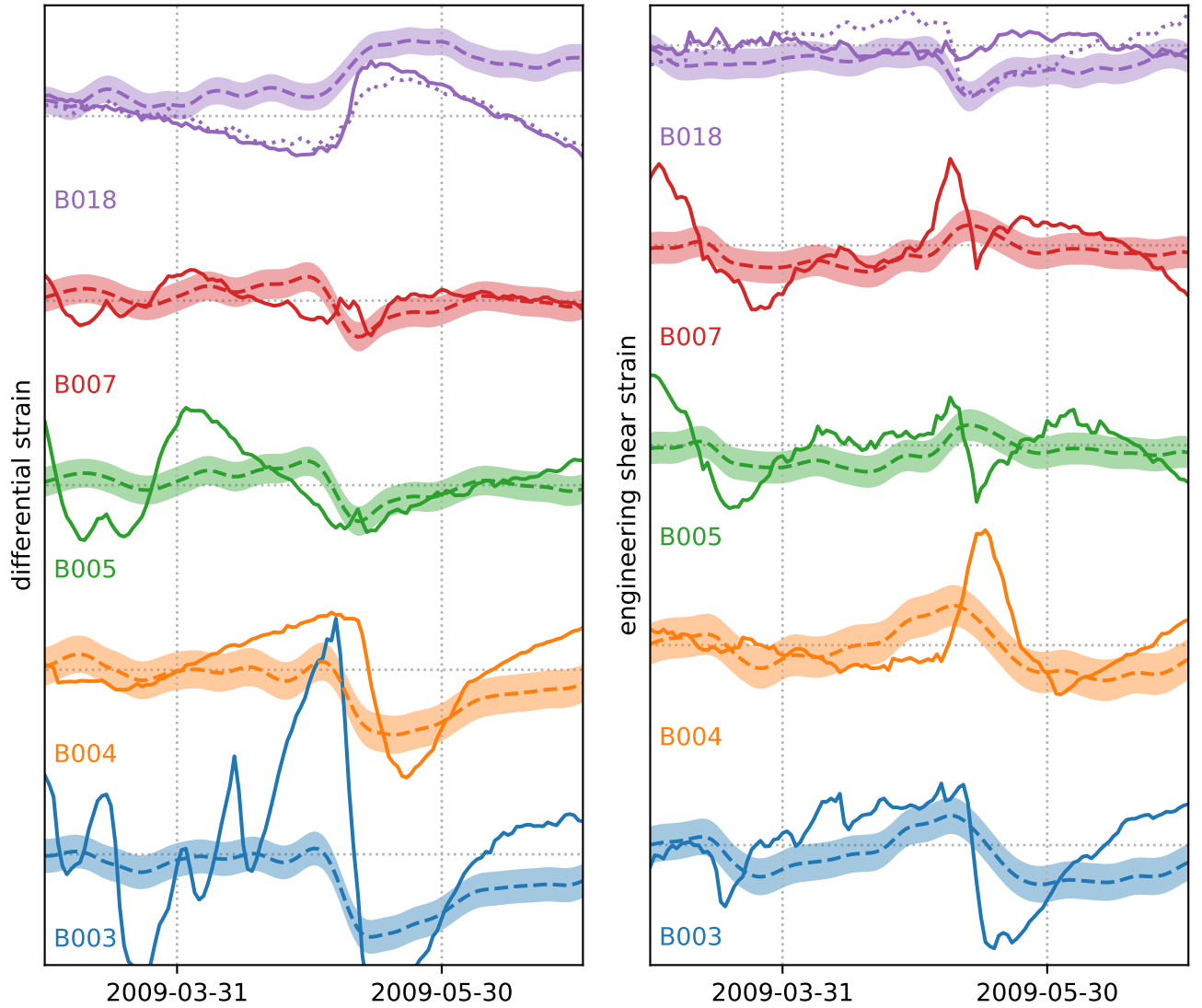
Figure 7: Same as Figure 2, but for the spring 2009 SSE.

Hart, R. H. G., Gladwin, M. T., Gwyther, R. L., Agnew, D. C., and Wyatt, F. K. (1996). Tidal calibration of borehole strain meters: Removing the effects of small-scale inhomogeneity. *Journal of Geophysical Research*, 101(96).

Hines, T. T. and Hetland, E. A. (2017). Revealing transient strain in geodetic data with Gaussian process regression. *submitted to Geophysical Journal International*, pages 1–25.

Hodgkinson, K., Agnew, D., and Roeloffs, E. (2013). Working With Strainmeter Data. *Eos, Transactions American Geophysical Union*, 94(9):91–91.

Langbein, J. (2015). Borehole strainmeter measurements spanning the 2014 Mw6.0 South Napa Earthquake, California: The effect from instrument calibration. *Journal of Geophysical Research B: Solid Earth*, 120(10):7190–7202.

Langbein, J., Murray, J. R., and Snyder, H. A. (2006). Coseismic and initial postseismic deformation from the 2004 Parkfield, California, earthquake, observed by global positioning system, electronic distance meter, creepmeters, and borehole strainmeters. *Bulletin of the Seismological Society of America*, 96(4 B):304–320.

Roeloffs, E. (2010). Tidal calibration of Plate Boundary Observatory borehole strainmeters: Roles of vertical and shear coupling. *Journal of Geophysical Research: Solid Earth*, 115(6):1–25.
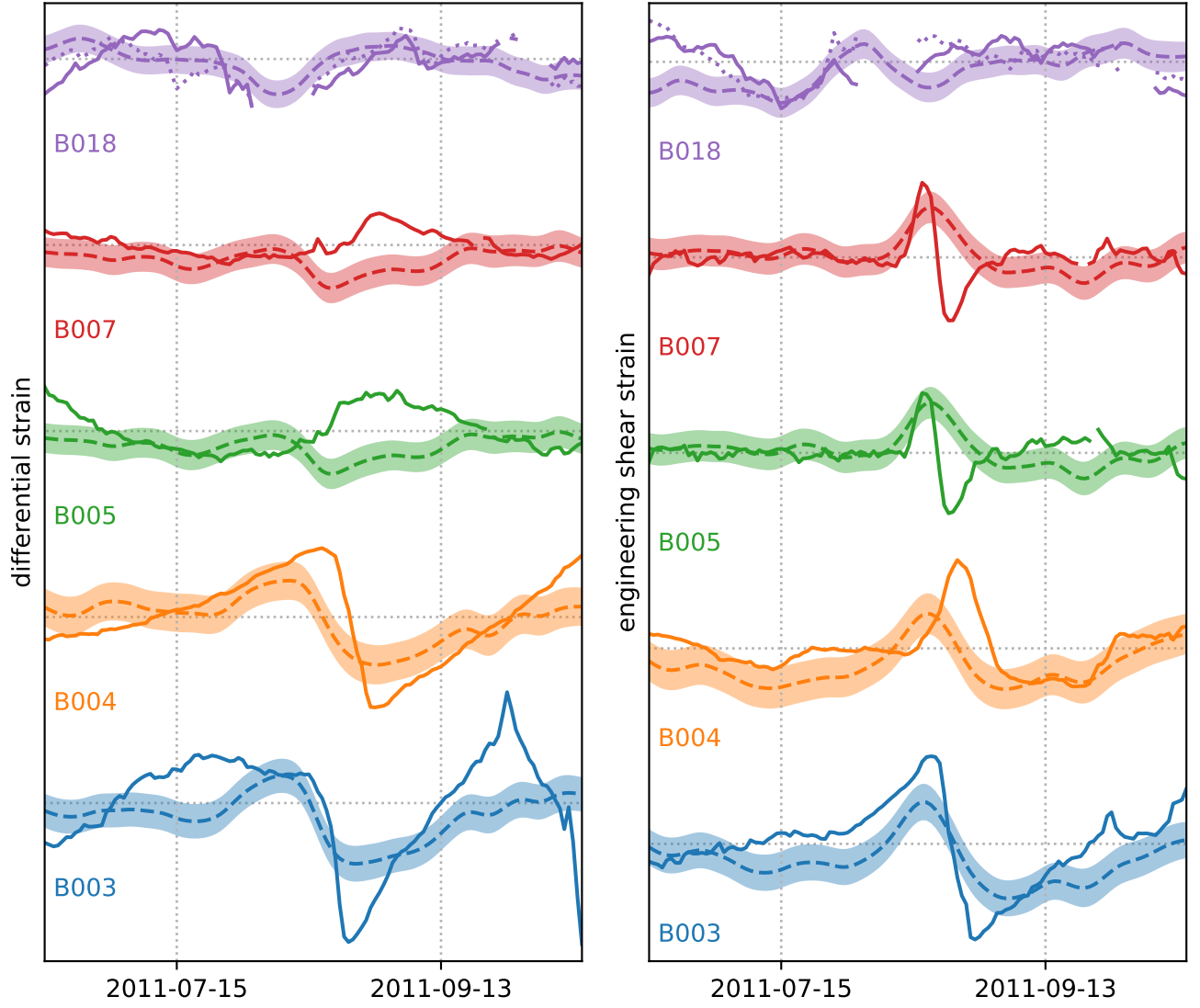
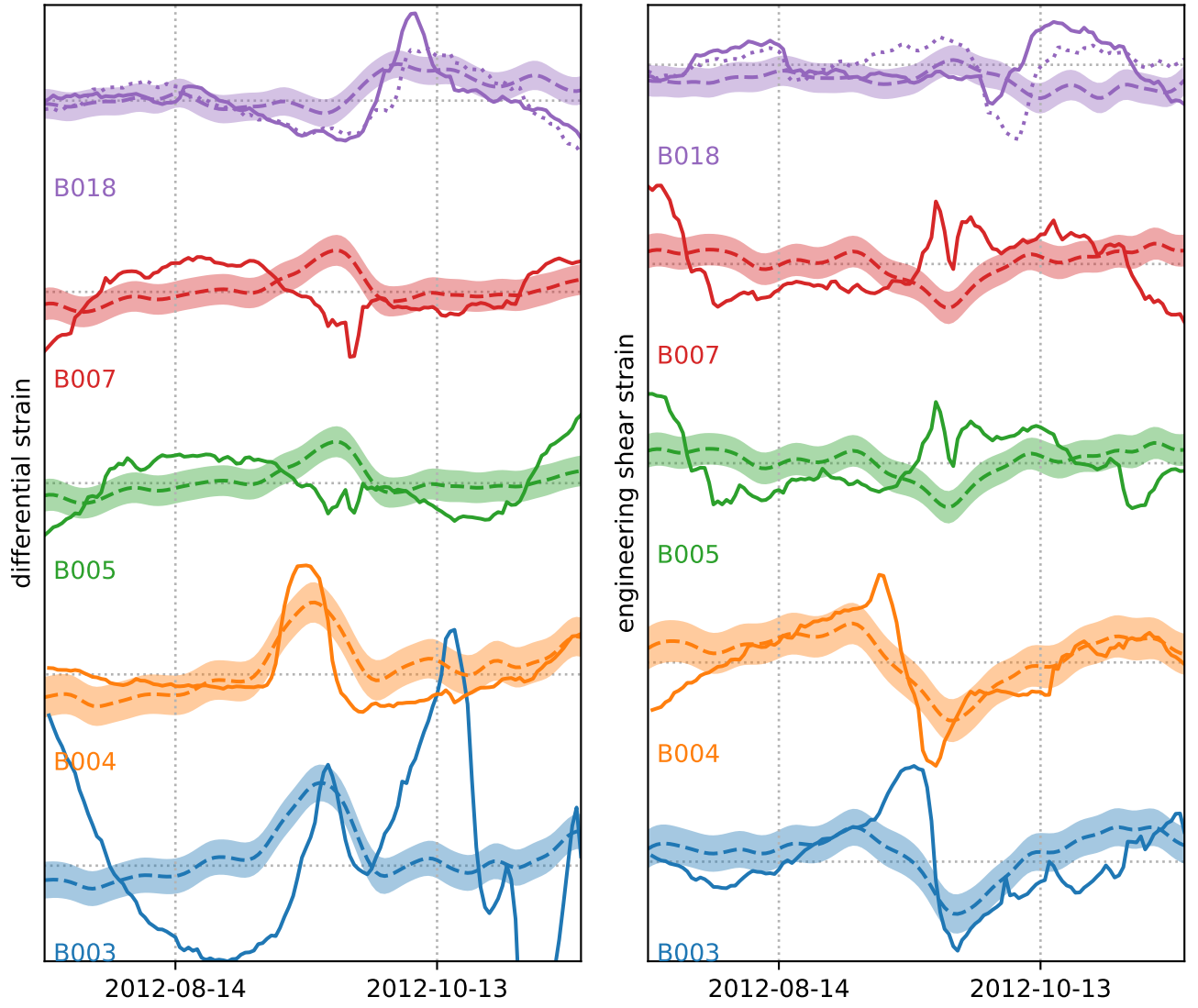Figure 8: Same as Figure 2, but for the summer 2011 SSE.

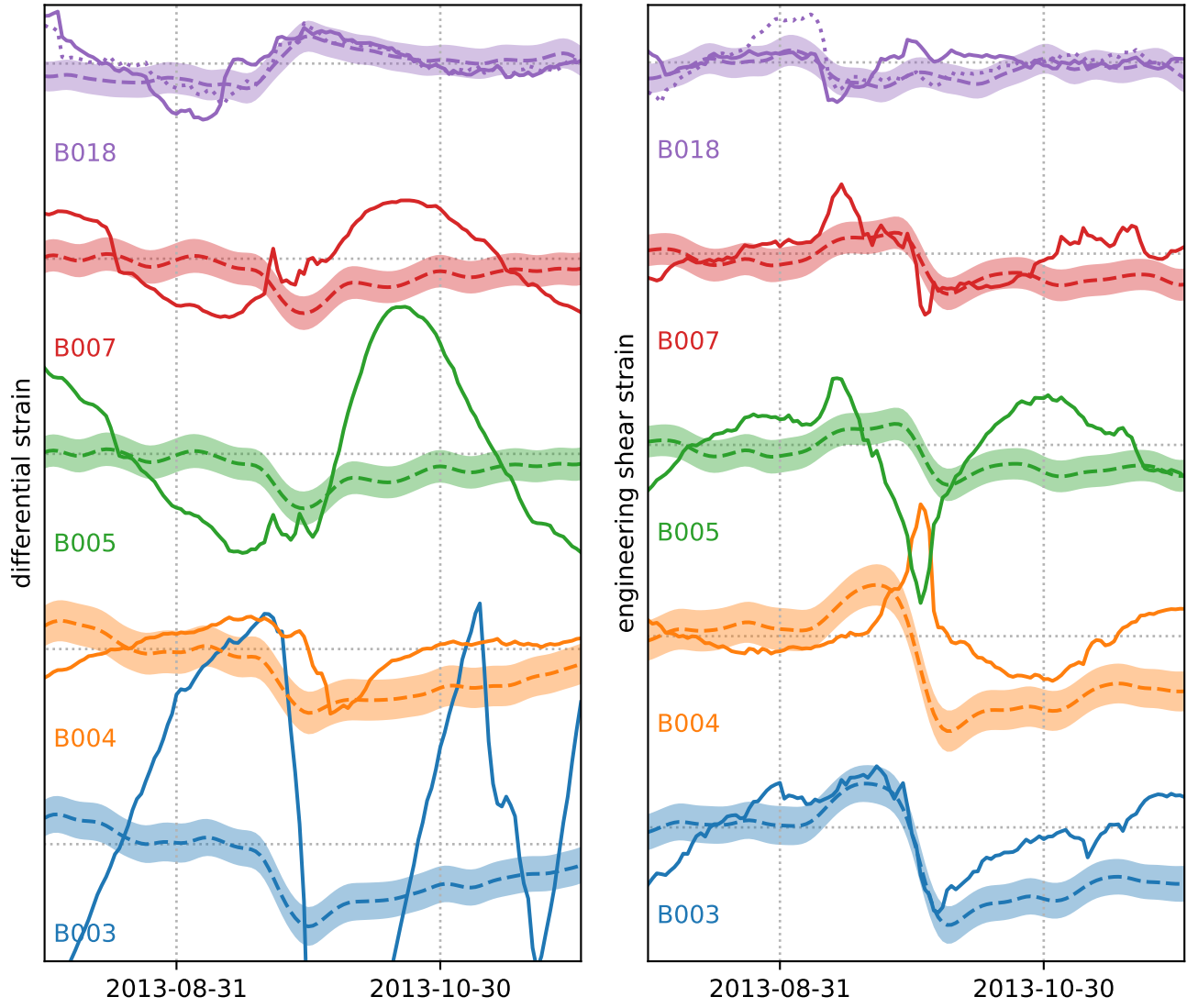Figure 9: Same as Figure 2, but for the summer 2012 SSE.

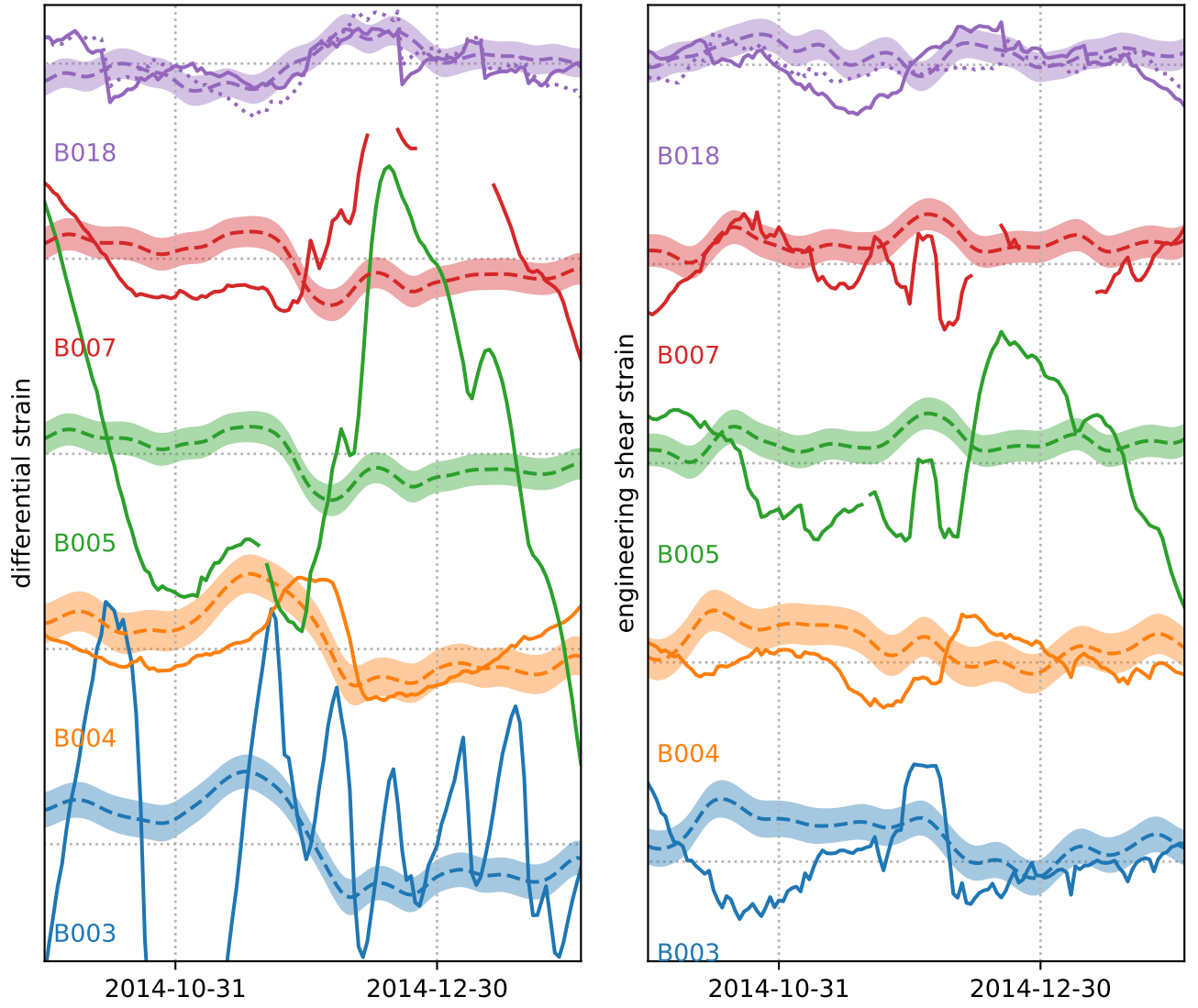Figure 10: Same as Figure 2, but for the fall 2013 SSE.

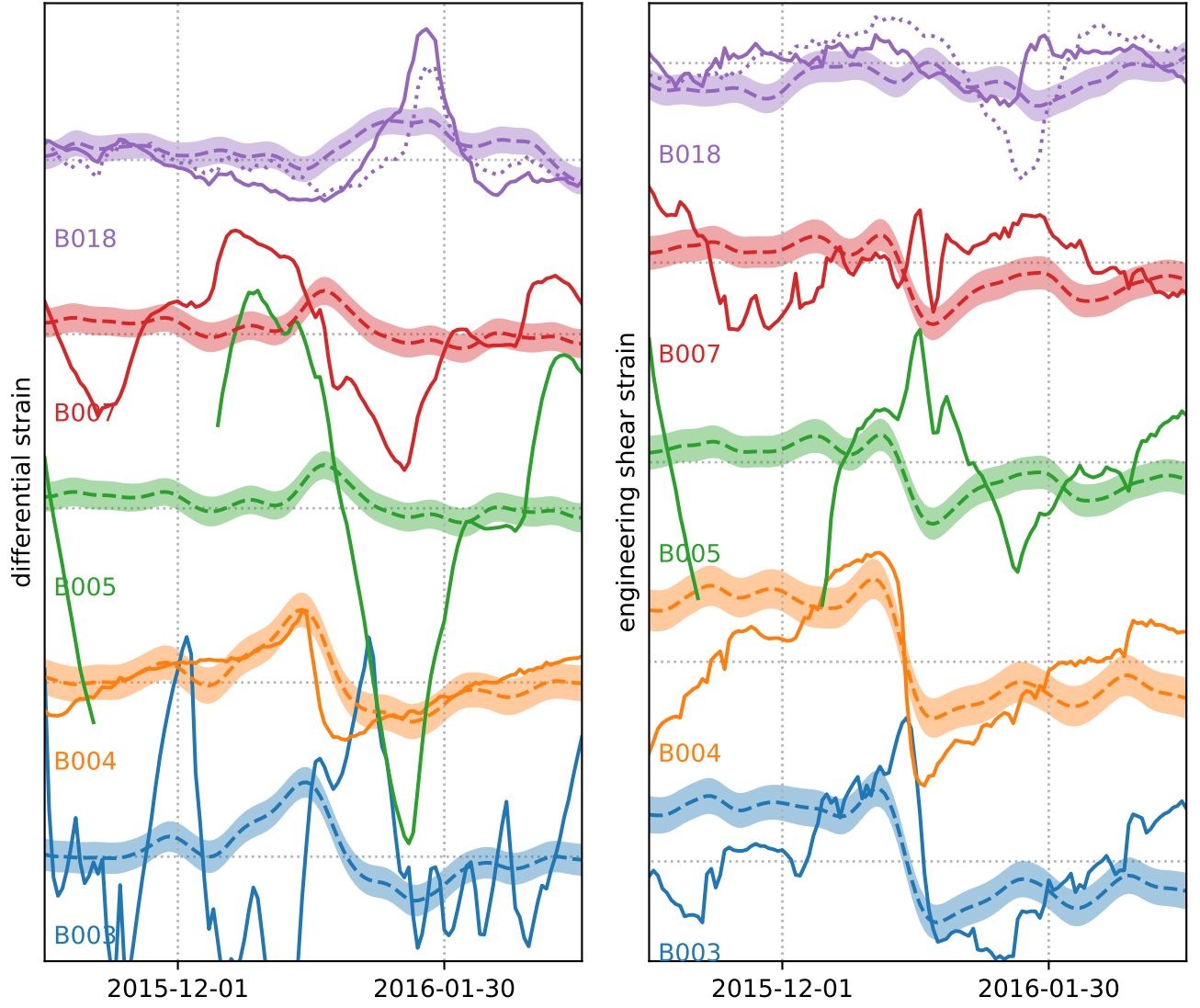Figure 11: Same as Figure 2, but for the fall 2014 SSE.
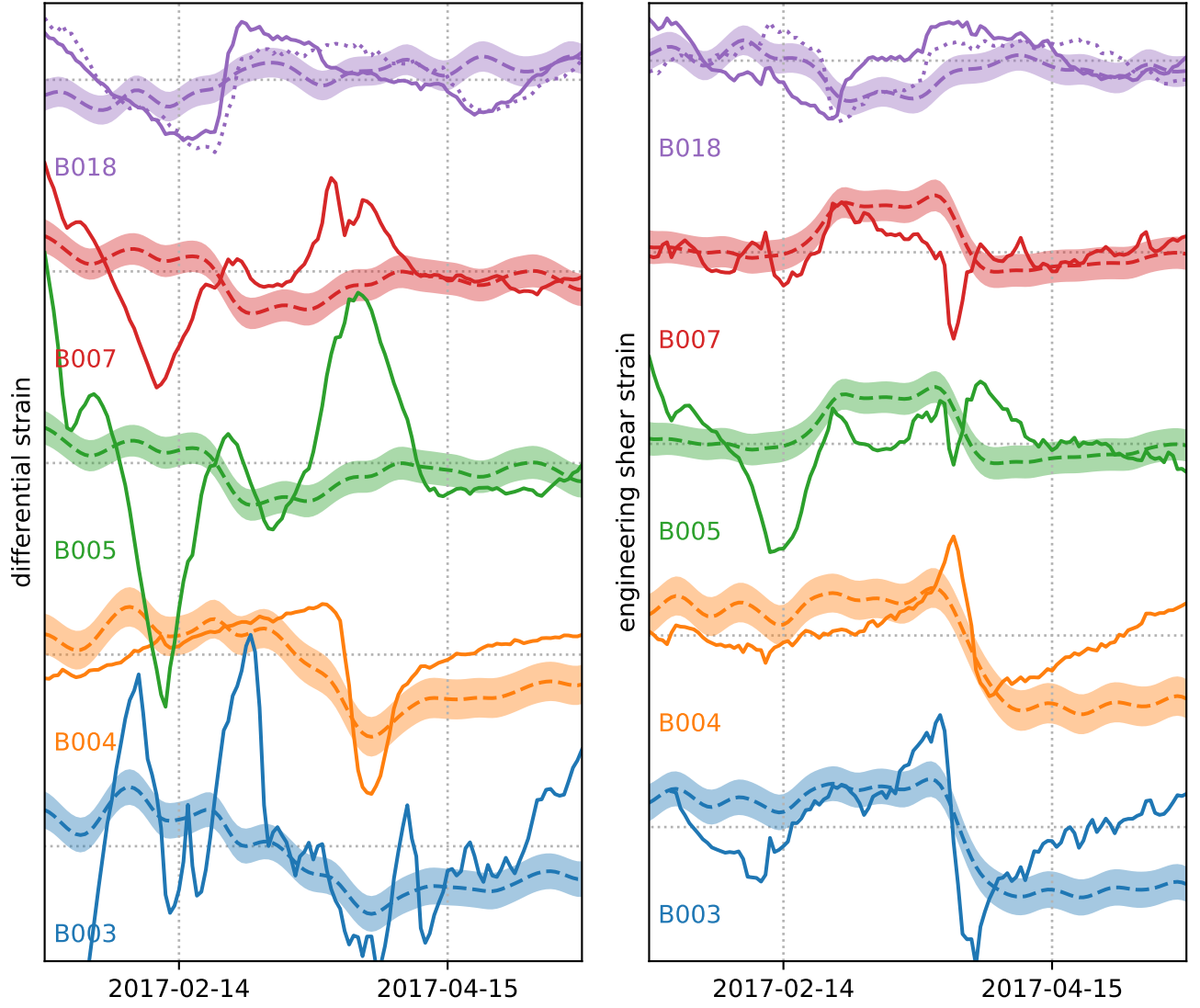
Figure 12: Same as Figure 2, but for the winter 2015-2016 SSE.

Figure 13: Same as Figure 2, but for the winter 2017 SSE.